




## Article

# Design of High-Gain and Low-Mutual-Coupling Multiple-Input–Multiple-Output Antennas Based on PRS for 28 GHz Applications

Jinkyu Jung <sup>1</sup>, Wahaj Abbas Awan <sup>1</sup> , Domin Choi <sup>1</sup>, Jaemin Lee <sup>1</sup>, Niamat Hussain <sup>2</sup>  and Nam Kim <sup>1,\*</sup> 

<sup>1</sup> Department of Information and Communication Engineering, Chungbuk National University, Cheongju 28644, Republic of Korea

<sup>2</sup> Department of Intelligent Mechatronics Engineering, Sejong University, Seoul 05006, Republic of Korea

\* Correspondence: namkim@chungbuk.ac.kr

**Abstract:** In this paper, a high-gain and low-mutual-coupling four-port Multiple Input Multiple Output (MIMO) antenna based on a Partially Reflective Surface (PRS) for 28 GHz applications is proposed. The antenna radiator is a circular-shaped patch with a circular slot and a pair of vias to secure a wide bandwidth ranging from 24.29 GHz to 28.45 GHz (15.77%). The targeted band has been allocated for several countries such as Korea, Europe, the United States, China, and Japan. The optimized antenna offers a peak gain of 8.77 dBi at 24.29 GHz with a gain of 6.78 dBi. A novel PRS is designed and loaded on the antenna for broadband and high-gain characteristics. With the PRS, the antenna offers a wide bandwidth from 23.67 GHz to 29 GHz (21%), and the gain is improved up to 11.4 dBi, showing an overall increase of about 3 dBi. A  $2 \times 2$  MIMO system is designed using the single-element antenna, which offers a bandwidth of 23.5 to 29 GHz (20%), and a maximum gain of 11.4 dBi. The MIMO antenna also exhibits a low mutual coupling of  $-35$  dB along with a low Envelope Correlation Coefficient and Channel Capacity Loss, making it a suitable candidate for future compact-sized mmWave MIMO systems.

**Keywords:** high gain; partially reflecting surface; MIMO antenna; 28 GHz; 5G; mmWave



**Citation:** Jung, J.; Awan, W.A.; Choi, D.; Lee, J.; Hussain, N.; Kim, N. Design of High-Gain and Low-Mutual-Coupling Multiple-Input–Multiple-Output Antennas Based on PRS for 28 GHz Applications. *Electronics* **2023**, *12*, 4286. <https://doi.org/10.3390/electronics12204286>

Academic Editor: Reza K. Aminenh

Received: 13 September 2023

Revised: 12 October 2023

Accepted: 13 October 2023

Published: 16 October 2023



**Copyright:** © 2023 by the authors. Licensee MDPI, Basel, Switzerland. This article is an open access article distributed under the terms and conditions of the Creative Commons Attribution (CC BY) license (<https://creativecommons.org/licenses/by/4.0/>).

## 1. Introduction

Mobile communication data traffic has shown a rapid surge soon after the introduction of Long-Term Evolution (LTE) to the public, thanks to a significant increase in communication device numbers. To meet the present requirements, the popularity of 5G mobile communication technology has risen. Research and development for advanced mobile communication technologies are currently in progress under the 5G umbrella, primarily due to its ability to offer higher data transmission rates per user in comparison to 4G technology. The 5G frequency spectrum consists of two main frequency bands: sub-6 GHz (3.5 GHz) and millimeter wave (mmWave) [1]. Among these, the mmWave frequency bands, which include representative bands like 28 GHz, 39 GHz, and 60 GHz within the 24 GHz to 100 GHz range, offer better reliability, lower delay rates, and faster communication speeds compared to sub-6 GHz [2]. Notably, the 28 GHz frequency has garnered significant attention due to its exceptional performance in comparison to other spectrum bands. This has led to South Korea allocating the range from 26.5 GHz to 28.9 GHz for mobile connectivity, while the European Union has been assigned frequencies ranging from 24.5 GHz to 27.5 GHz by ITU. Additionally, the 3GPP standard designates 24.25 GHz to 27.5 GHz for use in the United States, while the range reserved for mobile communication is 27.5 GHz to 28.35 GHz [3], as shown in Figure 1.

Countries	24 – 28 GHz band	37 – 40 GHz band	64 – 71 GHz band
Korea 🇰🇷	26.5 – 29.5 GHz		
Japan 🇯🇵	27.5 – 29.5 GHz		
Singapore 🇸🇬	24.25 – 26.5 GHz 26.5 – 27.5 GHz		
Canada 🇨🇦	27.5 – 28.35 GHz	37 – 40 GHz	64 – 71 GHz
USA 🇺🇸	24.75 – 25.25 GHz 27.5 – 28.35 GHz	37 – 40 GHz 47.2 – 48.2 GHz	64 – 71 GHz
UK 🇬🇧	26 GHz		
Germany 🇩🇪	26 GHz		
France 🇫🇷	26 GHz		
Italy 🇮🇹	26.5 – 27.5 GHz		
Sweden 🇸🇪	26.25 – 27.5 GHz		
Finland 🇫🇮	25.1 – 27.5 GHz		
China 🇨🇳	24.75 – 27.5 GHz	40 – 43.5 GHz	

Figure 1. Current status of mmWave frequency allocation in major countries [3].

Conversely, the trend towards smaller sizes for 5G devices has led to limited space for antenna systems. This is where millimeter-wave antennas have an edge over traditional sub-6 GHz antennas, as they do not require as much space. However, the mmWaves are not very resilient to the surrounding environment and have poor performance in non-line-of-sight scenarios [4]. Researchers have found that this limitation of the mmWave band spectrum can be overcome by designing higher gain antennas along with Multiple-Input-Multiple-Output (MIMO) capabilities. The MIMO systems offer numerous advantages over Single-Input-Single-Output (SISO) that are not limited to lower power consumption, improved signal range, reduced bit errors that result in reduced interference and enhanced NLOS connectivity [5]. Moreover, an effective MIMO antenna system should not only provide a compact size and high gain, but also excel in terms of factors like mutual coupling, efficiency, Envelop Correlation Coefficient (ECC), Channel Capacity Loss (CLL), and various diversity parameters including Diversity Gain [6–10]. As a result, numerous recent articles in the literature have explored different techniques to meet the growing demands for 5G millimeter-wave MIMO antenna systems.

As an example, a researcher developed an MIMO antenna enhanced with a ground stub to diminish mutual coupling [9]. They also employed a metasurface to mitigate mutual coupling between closely positioned elements. However, this approach led to increased dimensions of 31 mm × 48 mm. Another notable study is documented in [11], where researchers designed a series array antenna in a rectangular patch shape for 28 GHz applications. This antenna covers a broad frequency range of 27.6–29.1 GHz, boasting a high gain of 10.2 dBi and minimal mutual coupling of >−40 dB. Nevertheless, the utilization of a slot array technique makes the antenna larger in size.

A different approach involves the design of a low-mutual-coupling MIMO antenna employing orthogonally positioned elements in the infinity shell shape [12]. While this proposed antenna benefits from its compact size, it still faces various challenges, including low gain, limited bandwidth, and the absence of a common ground plane in its design, rendering it less suitable for practical applications. Similarly, [13] introduces an MIMO antenna based on a dielectric resonator. This design achieves a mutual coupling of >−24 dB within the frequency range of 25.2–28 GHz. However, the gain remains low for 5G applications.

In contrast to the works mentioned earlier, a flat-lens antenna is developed using an ultrathin Huygens' metasurface, aiming to achieve a high gain of 30 dBi [14]. However, the limitation of such antennas lies in their exceptionally large size, which confines their application to either measurement setups or military purposes where size constraints are not a concern.

On the other hand, a four-element MIMO antenna designed for a 28 GHz application employs a two-element array configuration as a single element [15]. This approach of using a two-element array aims to achieve a higher gain and broader bandwidth compared to a single-element design. Additionally, the antenna employs a defected ground structure technique along with orthogonal placement to achieve reduced mutual coupling between adjacent elements. The resulting antenna covers a wide frequency range of 25.5–29.6 GHz, exhibiting a moderate coupling of  $> -18$  dB and a gain of 8.3 dBi.

Research efforts by [10,16] concentrate on enhancing the MIMO antenna by adding an extra layer of metasurface. For the four-element MIMO antenna with an orthogonal placement, introducing a metasurface at the back of the antenna enhances the gain from 6 dBi to 10 dBi [10]. However, the bandwidth and mutual coupling among elements remain consistent with the MIMO antenna lacking a metasurface. Conversely, [16] fully exploits the metasurface-loading technique to achieve both a wide bandwidth and high gain. This leads to a bandwidth improvement of 5.5 GHz, spanning 23.3–28.8 GHz and a gain increase of 4 dBi, resulting in a peak gain of 10.21 dBi. It is noteworthy that a maximum mutual coupling of  $-22.5$  dB is observed at the operational frequency.

Another intriguing study is documented in [17], where a multilayered antenna based on a chiral metasurface is devised. This antenna offers the advantage of improved performance in terms of bandwidth, high gain, and reduced mutual coupling. However, it does face certain challenges, including structural complexity due to its multiple layers and elevated profile.

Based on the aforementioned considerations, it becomes evident that a pressing need exists for a mmWave MIMO antenna capable of delivering a superior performance across all parameters, while still maintaining a compact size, structural simplicity, and strong diversity performance. Therefore, this paper presents the design of an MIMO antenna characterized by its compact dimensions, low mutual coupling, high gain, and robust MIMO performance metrics.

The manuscript is organized as follows: Section 2 outlines the design process and outcomes for both the single antenna element and the MIMO antenna, along with their respective performance parameters. Section 3 details the design procedure for the metasurface and its integration with the antenna, along with an examination of various performance metrics. The concluding section, Section 4, provides a comparison between the proposed work and existing literature.

## 2. Antenna Design

The geometric representation of the proposed MIMO antenna system is depicted in Figure 2. This MIMO antenna comprises four circular patch antennas, each featuring a semi-circular slot and a pair of vias. In order to achieve minimal mutual coupling, these elements are positioned orthogonally to each other, as illustrated in Figure 2a. The MIMO antenna is backed by a full copper ground plane, as displayed in Figure 2b. For the simulation setup, the antenna is made using copper and the ROGERS 5880 substrate. The exact properties are assigned to all materials. The radiation box is placed at a quarter wavelength in all directions from the antenna system, where a central frequency of 28 GHz is chosen for the wavelength calculation. Air is assigned as a material for the radiation box.

For an additional enhancement of the proposed MIMO system's performance, a partially reflecting surface is incorporated. This surface consists of a  $6 \times 6$  array of meta cells, where each meta cell is designed with a staircase-like structure on the upper side, as seen in Figure 2c, and a square loop on the reverse side, as depicted in Figure 2d. Placed atop the antenna with an airgap of  $G$ , this metasurface is shown in Figure 2e. Maintaining uniform dimensions of  $24 \times 24$  mm<sup>2</sup> for both the antenna and metasurface facilitates the measurement setup.

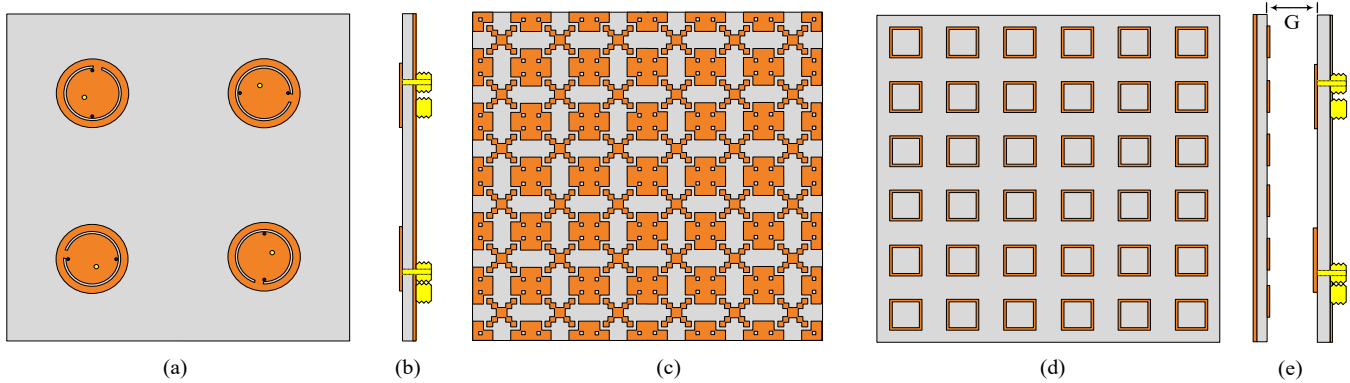


**Figure 2.** The proposed MIMO antenna with PRS. (a) Front view of MIMO antenna, (b) side view of MIMO antenna, (c) front view of PRS, (d) back view of PRS, (e) side view of MIMO antenna with PRS.

### 2.1. Single-Element Antenna Design

The proposed approach involves four sequential steps, commencing with the design of a circular patch antenna, followed by the creation of two distinct models utilizing a slot and a pair of vias. These models are subsequently merged and optimized to yield the ultimate broadband antenna.

The selection of the circular patch antenna stems from its numerous advantages, including its compact size, compatibility with array structures, and microwave monolithic integrated circuits. Furthermore, circular patch antennas can be seamlessly integrated into both planar and non-planar configurations.

The resonant frequency of the circular patch is determined by its radius ( $r$ ), while impedance matching can be managed by optimizing the positioning of the feeding pin. The radius at the desired frequency can be extracted using the following formula [18]:

$$r = \frac{F}{1 + \frac{2h}{\pi\epsilon_r F} \left[ \ln \frac{\pi F}{2h} + 1.7726 \right]^{\frac{1}{2}}} \quad (1)$$

Here, the  $\epsilon_r$  refers to the dielectric constant of the substrate,  $h$  denotes the substrate thickness, while  $F$  is the constant, which can be estimated in terms of the resonating frequency by the mean of the following expression [18]:

$$F = \frac{8.791 \times 10^9}{f_r \sqrt{\epsilon_r}} \quad (2)$$

The antenna is designed using RT5880 by ROGERS corp., having low dielectric value and low loss. The pin position is optimized for good impedance matching at a center frequency of 26 GHz, as shown in Figure 3. The circular patch offers bandwidth ranges 25.6–27.25 GHz, as depicted in Figure 4a.

In order to extend the bandwidth to encompass the entire globally allocated 5G frequency spectrum, the technique of etching slots and employing loading vias is employed. In the first scenario, a semi-circular slot is etched from the radius, as demonstrated in Figure 3. This leads to a redistribution of surface currents, resulting in a broader bandwidth of 25.37–27.05 GHz, as depicted in Figure 4.

In the second scenario, a pair of vias is loaded to reduce the length of the radiating structure in connection with the ground. This introduces added resistance to the radiator, which in turn facilitates impedance matching across a wider frequency range of 25.3–28.5 GHz, as displayed in Figure 4a. However, while both antenna-2 and antenna-3 exhibit a wider bandwidth compared to antenna-1, neither covers the desired frequency band. Consequently, both antennas were integrated, as presented in Figure 3.

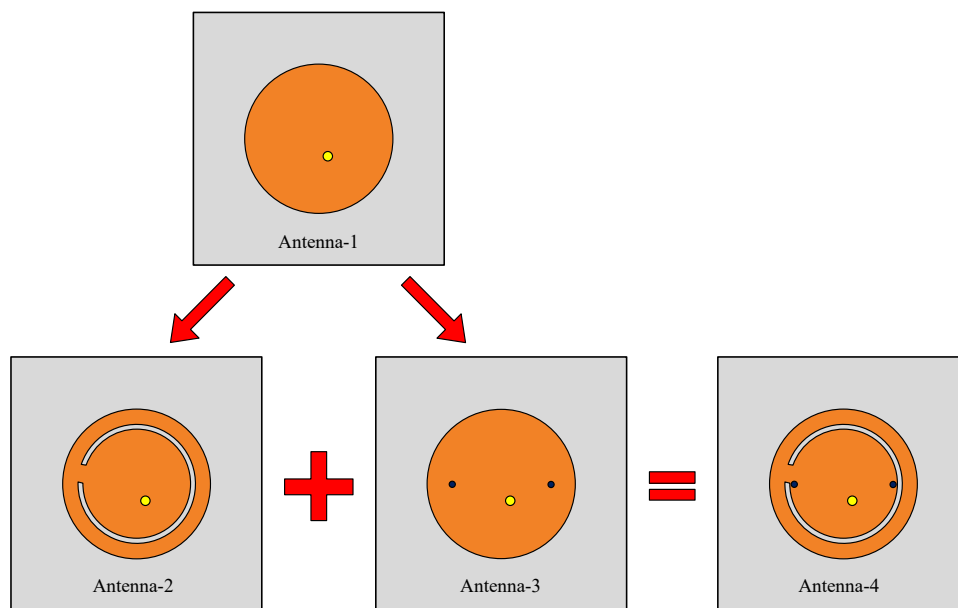


Figure 3. Design evolution of proposed circular patch antenna.

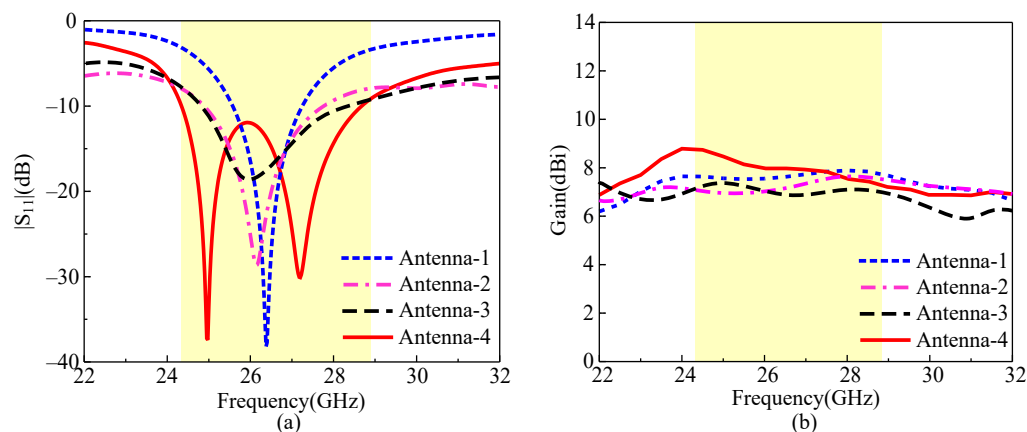
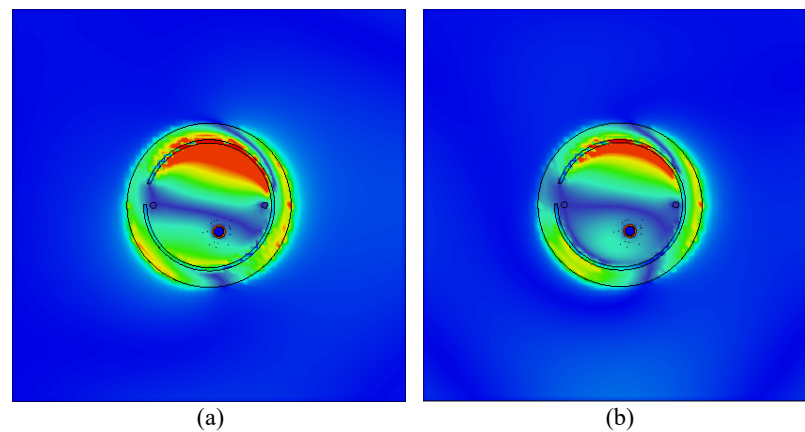


Figure 4. Performance comparison of the various antenna designs (a)  $|S_{11}|$  and (b) gain.

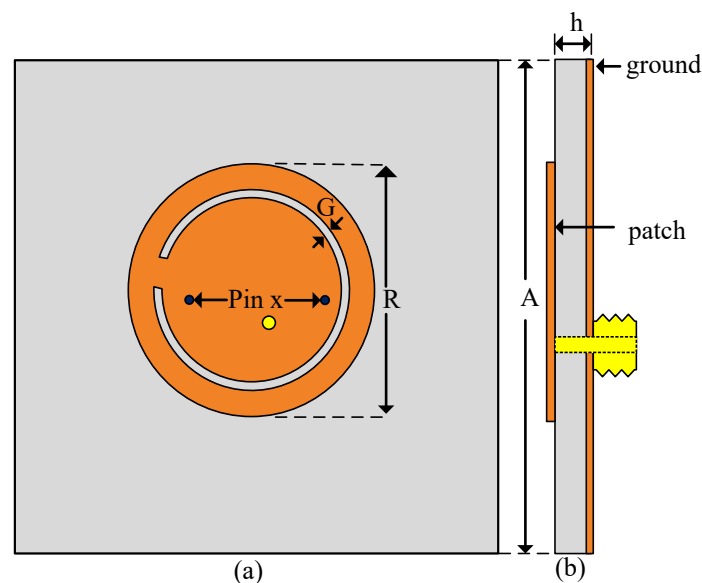
This integrated antenna results in the generation of a broad frequency range spanning 24.29–28.45 GHz, featuring two resonances at 25 GHz and 27 GHz. The occurrence of these resonances is attributed to the interplay of the slot and the via, resulting in distinct electrical lengths with respect to the feeding point. Furthermore, Figure 4b illustrates a comparison between the basic antenna and the final integrated antenna, confirming a marginal enhancement in the peak gain of the antenna. To further understand the broad impedance bandwidth mechanism, the surface current distribution is illustrated in Figure 5. The current is distributed along the inner patch as well as the outer patch with respect to the slot for the 25 GHz band, which refers to a bigger electrical length. On the other hand, for 27 GHz, the current is mainly distributed along the inner patch while the small amount of current at the outer patch also shows that it takes part in achieving higher resonance. The antenna configuration is shown in Figure 6, while the values of various optimized parameters are listed in Table 1.

Table 1. Optimized parameters of proposed antenna.

Parameter	A	Pin x	G	R	h
Length (mm)	12	3.2	0.1	2.5	0.787



**Figure 5.** Current distribution of the optimized antenna at (a) 25 GHz and (b) 27 GHz.



**Figure 6.** Geometrical illustration of proposed mmWave wideband single-element antenna. (a) Top view and (b) side view.

## 2.2. Partial Reflective Surface Design

Despite the antenna demonstrating commendable performance in terms of bandwidth and gain, there remains a need for performance enhancement due to the relatively low energy possessed by mmWave. This is particularly crucial to counteract the atmospheric absorption losses. To address this, the gain must be enhanced to mitigate such losses. In pursuit of this objective, metamaterials with unique attributes not commonly found in other materials are designed and integrated alongside the antenna.

Metamaterials are categorized into several types based on their working principles and behaviors, including frequency selective surfaces (FSSs), electronic bandgaps (EBGs), and partial reflective surfaces (PRSs). FSSs are typically paired with monopole antennas, positioned at the rear side to reduce rearward radiation. However, an FSS has limitations, such as its larger volume and constraints when applied in compact devices. Conversely, EBG structures find their use between MIMO antenna elements to diminish mutual coupling, thus enhancing the signal strength.

PRS refers to a reflecting surface with varying reflection characteristics based on the incident frequency angle, polarization, or radio wave band. It is often chosen for its significant impact on gain improvement. When employed in this manner, it is mainly positioned in front of the antenna, functioning as a resonator along with the antenna's ground surface, forming a Fabry–Perot (FP) resonator. For the antenna with a PRS antenna,

a substantial gain can be achieved in the direction of propagation. An advantageous aspect of the FP resonance antenna is its relatively uncomplicated structure, offering the potential for high gains. However, the FP resonator also has its downside, featuring a narrow impedance and radiated bandwidth due to resonance conditions being met at a single frequency.

In light of these considerations, research has been directed toward maximizing the high-gain advantage of PRS while addressing the limitation of bandwidth narrowness.

Thus, instead of designing the PRS structure on the single side of the substrate, a dual sided structure is utilized to achieve a wideband operation. The back side of the PRS unit cell contains a square loop structure, while the front side is modified using various steps, as shown in Figure 7. Initially, a full copper-covered side is used, which is then converted to a marble-like structure by etching four rectangular slots from it. Afterwards, more structural changes are carried out by etching slots from the corner patches, and rotating the middle structure after etching slots from the middle patch. Finally, small square slots are extracted from the corner patches, while small rectangular patches are added at the corner of the middle structure.

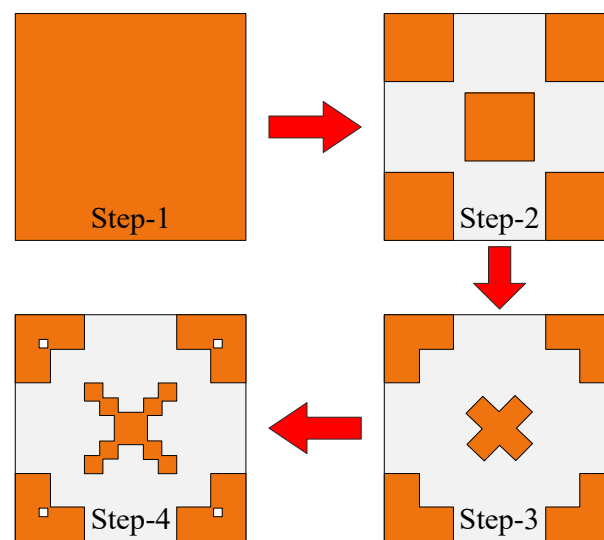


Figure 7. Design evolution of proposed PRS.

In the electromagnetic theory, the metasurface modifies electromagnetic waves through specific boundary conditions as opposed to the three-dimensional (3D) space's construction parameters, which are frequently used in meta-materials and follow similar PRS principles. Using CST Studio's unit cell designing tool, the reflection coefficient and phase are analyzed considering general incidence and by using the open boundary condition on the xy plane of the cell.

Figure 8 shows the reflection coefficient and phase results of the optimized PRS. The reflection coefficient and phase are crucial key parameters in designing a wideband with a high-gain mmWave antenna. A higher reflective PRS leads to a higher gain, but narrower  $-3$  dB bandwidth; to broaden this, a PRS with a positive phase gradient is used. The resulting reflection coefficient and phase of the optimized PRS have a positive gradient and almost exactly resemble the ideal phase of the PRS over a wide-bandwidth spectrum range.

Figure 9 presents the design of the proposed PRS unit cell, along with optimized parameters for various dimensions.

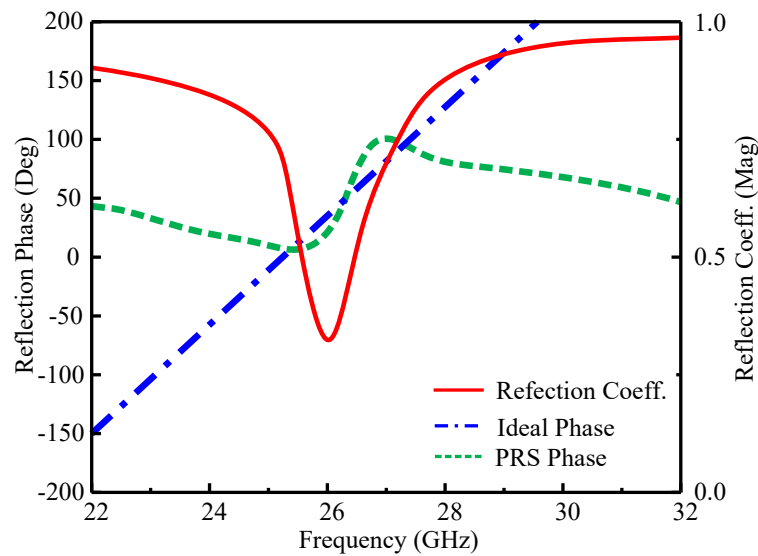


Figure 8. Reflection coefficient’s magnitude and phase of the optimized PRS unit cell.

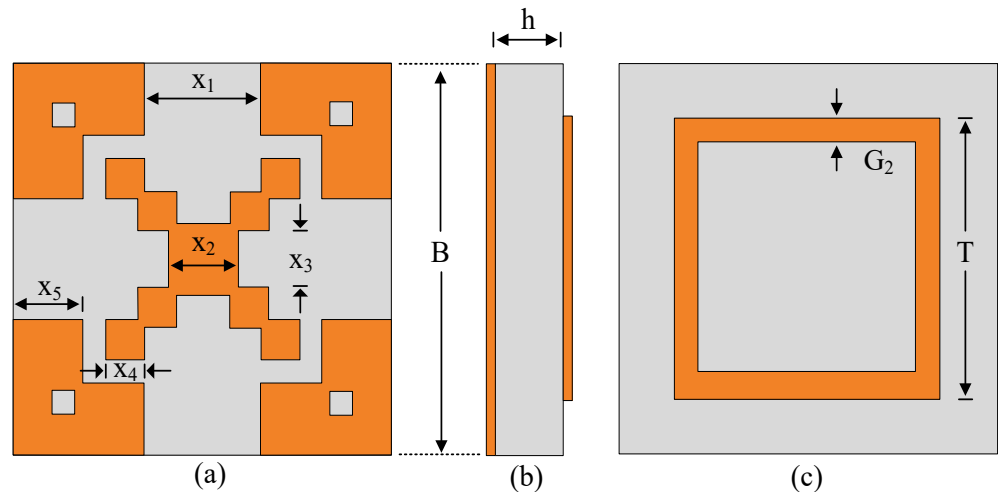


Figure 9. Proposed PRS unit cell: (a) top view, (b) side view, (c) bottom view. Parameter:  $B = 12$ ;  $T = 3.2$ ;  $G_2 = 0.1$ ;  $h = 0.787$ ;  $x_1 = 1.22$ ;  $x_2 = 0.73$ ;  $x_3 = 0.73$ ;  $x_4 = 0.4$ ;  $x_5 = 0.73$  (units are in mm).

### 2.3. PRS-Loaded Single-Element Antenna

The PRS is loaded on the top side of the antenna, as shown in Figure 10. The Ray theory explains that the vector sum of the partially transmitted electromagnetic waves results in an electric field which is given by the following relation [19]:

$$TE = \sum_{j=-\infty}^{\infty} f(\theta)E_j \tag{3}$$

where  $f(\theta)$  denotes the radiated field pattern generated by the source having an angle  $(\theta)$ , while  $E_j$  denotes the reflected field as the collective sum of the vector field by the reflector and metasurface. To obtain the maximum power transmitted towards the broadside, the following resonance condition must be met.

$$\psi - \pi - \frac{4\pi G_3}{\lambda_0} = 2N\pi \tag{4}$$



where  $\lambda_0$  denotes the free-space wavelength at the central frequency of the antenna;  $N$  will be an integer, while the  $G3$  represents the gap among the antenna and PRS, which must satisfy the following relation:

$$G3 = \left( \frac{\psi}{360} - 0.5 \right) \frac{\lambda_0}{2} - N \frac{\lambda_0}{2} \tag{5}$$

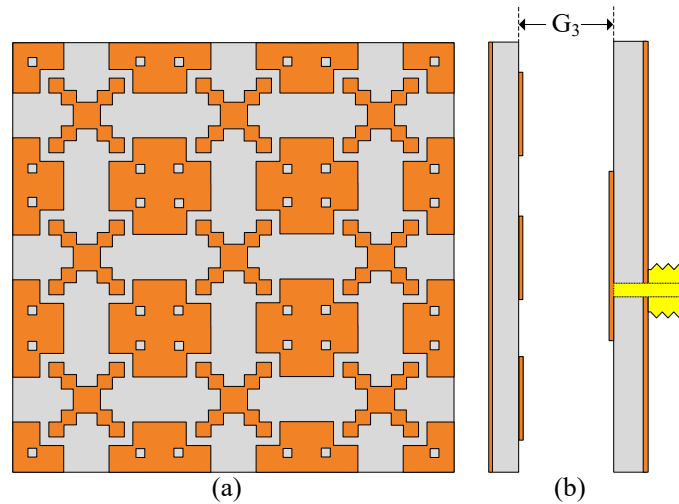


Figure 10. Single antenna with PRS: (a) top view, (b) side view.

However, due to a loss of materials, the gap between the PRS and antenna needs optimization. For said purpose, the parametric analysis is carried out and based upon the return loss, and the gain performance of the optimized gap is found to be 5.8 mm. Figure 11a shows the  $|S_{11}|$  results of the antenna before and after loading PRS; the impedance bandwidth is improved from 4.16 GHz to 5.27 GHz with a range of 23.63–28.9 GHz. Similarly, the gain of the antenna significantly improved when loaded with the metasurface; an average gain improvement of 3 dBi is observed for the operational bandwidth, as shown in Figure 11b.

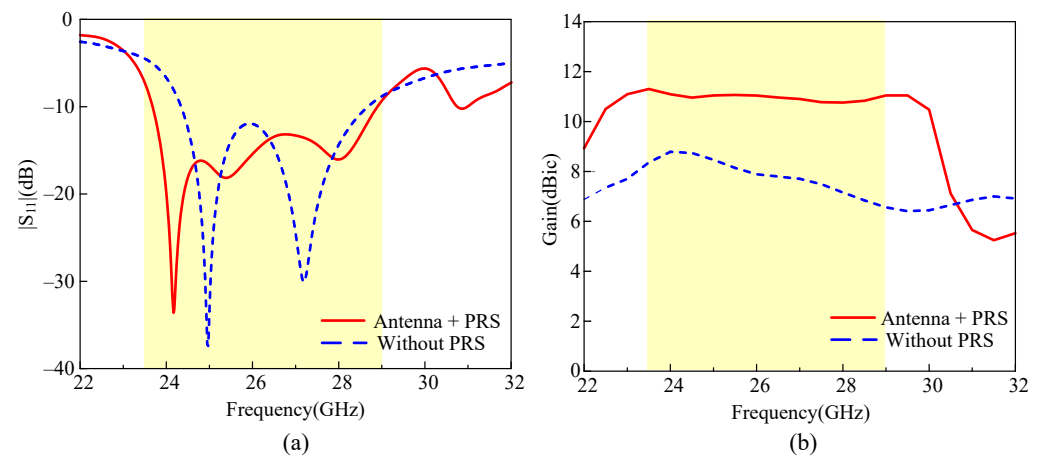


Figure 11. Single-element antenna with PRS performance; (a) S11 parameter, (b) gain.

#### 2.4. PRS-Loaded MIMO Antenna

MIMO antennas leverage spatial diversity and spatial multiplexing techniques and offer multipath propagation through multiple antennas, resulting in elevated transmission rates; robust signals are less susceptible to attenuation or loss, ensuring stable communication [20]. However, the mutual coupling among MIMO antenna elements can disrupt system performance. As a result, MIMO antennas require minimal mutual coupling among elements to function effectively.

The fundamental antenna design from the preceding section serves as the foundation for constructing a four-element MIMO antenna. Orthogonal placement is employed to achieve low coupling among the elements, eliminating the need for additional decoupling structures. It is important to note that, due to measurement constraints and the size limitations of mmWave connectors, inter-spacing cannot be reduced.

Figure 12 shows the geometrical configuration of the MIMO antenna with interspace among adjacent antennas of  $w = 7$  mm, referring to  $\lambda/2$  at the lowest resonance. The total size of the antenna is  $24 \times 24$  mm<sup>2</sup>, which is twice the size of a single-element antenna. As stated earlier, the PRS is loaded to achieve a high gain; so, a  $9 \times 9$  array of meta-cells is loaded on the topside of the MIMO antenna while keeping the same gap as that utilized for a single element, as shown in Figure 10.

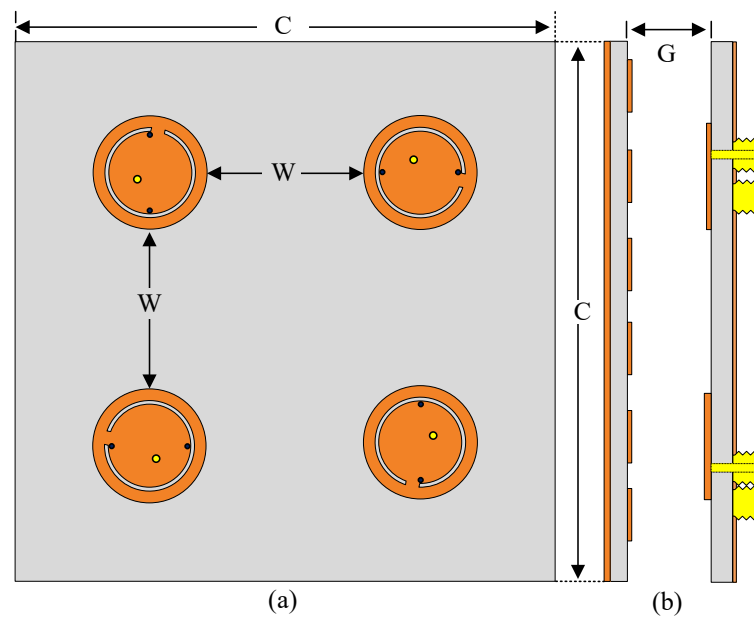


Figure 12. PRS-loaded MIMO antenna: (a) top view (b) side view.

Figure 13 shows the s-parameter performance of the proposed PRS-loaded MIMO antenna.

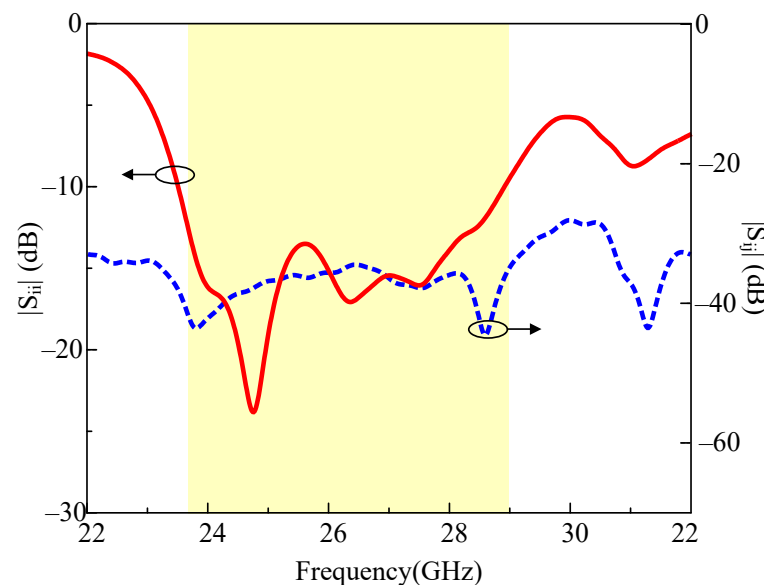


Figure 13. S-parameters of the proposed PRS-loaded MIMO antenna.

It is observed that the antenna offers an  $|S_{11}| > -10$  dB impedance bandwidth of 5.5 GHz, starting from 23.5 GHz to 29 GHz. Moreover, the mutual coupling of  $> -33$  dB is achieved throughout the operational region.

### 3. Results and Discussion

#### 3.1. Fabrication and Measurement

To validate the findings presented in the preceding section, a prototype of the antenna and metasurface was fabricated and subjected to testing. In Figure 14a, the different components of the PRS-loaded antenna and its MIMO configuration are depicted, while the complete setup, including the use of polyurethane foam to create a gap between the PRS and the antenna, is illustrated in Figure 14b.

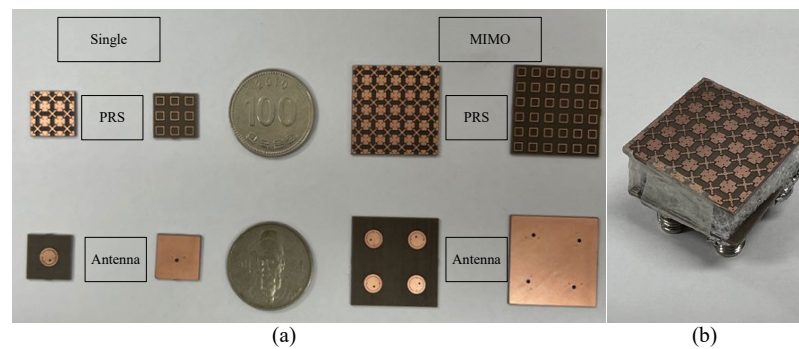


**Figure 14.** Manufactured  $2 \times 2$  MIMO antenna photographs: (a) parts of each MIMO, (b) manufactured prototype.

The evaluation of radiation patterns and gain measurements was conducted within a newly established circular chamber, as shown in Figure 15. Further details regarding the functioning of the circular chamber and its superior efficiency compared to traditional mmWave far-field chambers can be found in [21].

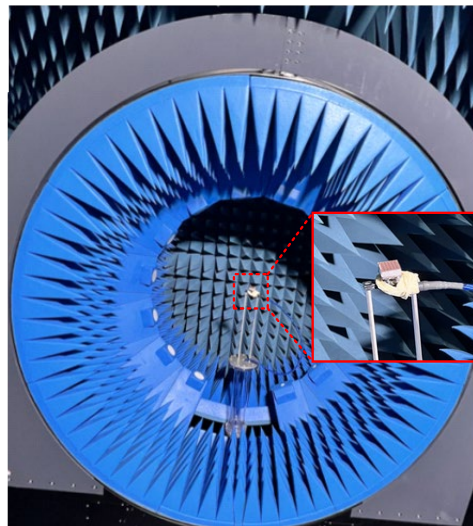


**Figure 15.** Snaps of the proposed MIMO antenna with PRS in the anechoic chamber.

#### 3.2. S-Parameter

The comparison among simulated and measured s-parameters is shown in Figure 16. The  $|S_{11}|$  results of the single-element antenna loaded with PRS and that of MIMO remain changed; thus, they included are not included separately. The measured results offer wideband ranges 23.5 GHz to 30 GHz, while the simulation results have the operational band of 23.5 GHz to 29 GHz, as shown in Figure 16a. On the other hand, Figure 16b shows mutual coupling among the MIMO elements where both simulated and measured results

offer a low mutual coupling of  $>-30$  dB. A strong performance in terms of comparison is obtained; however, the discrepancy between the results may be due to fabrication and measurement setup tolerance [22].

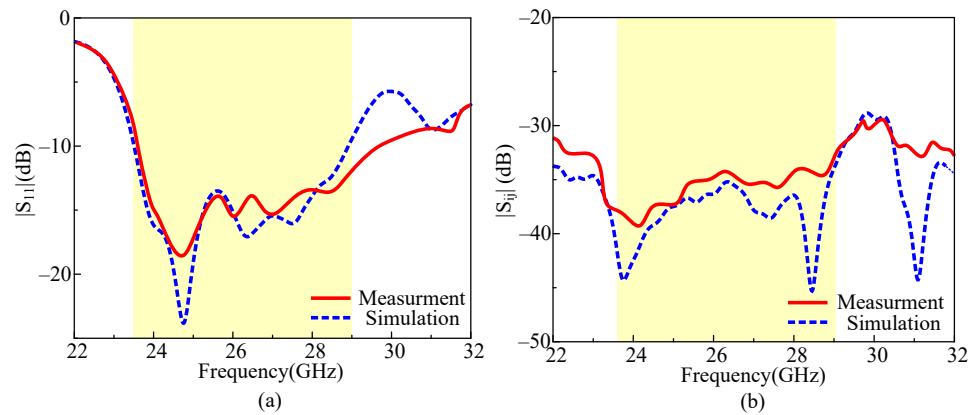


**Figure 16.** Comparison of simulation and measurement data of fabricated prototypes; (a) is  $|S_{11}|$  and (b) is  $|S_{12}|$ .

### 3.3. Radiation Pattern

The radiation patterns of the proposed PRS-loaded MIMO antenna are measured; the comparison with simulated results is shown in Figure 17. Since measurement was conducted from 26.5 GHz due to the limitation of the measuring equipment, the result value of 26.5 GHz was attached, not the center frequency of 26 GHz. In both principal E- and H-planes, the antenna exhibits a broadside radiation pattern. At 26 GHz, the antenna exhibits a slightly titled radiation pattern in E-plane, which has the maximum value of radiation at  $\theta = 15^\circ$ , as shown in Figure 17a. Likewise, in H-plane, the antenna offers peak radiation at  $\theta = 25^\circ$  for 26 GHz, as shown in Figure 17b. On the other hand, the PRS-loaded antenna offers peak radiation toward  $\theta = 0^\circ$  for both E- and H-planes at the resonating frequency of 28 GHz, as shown in Figure 17a,b.

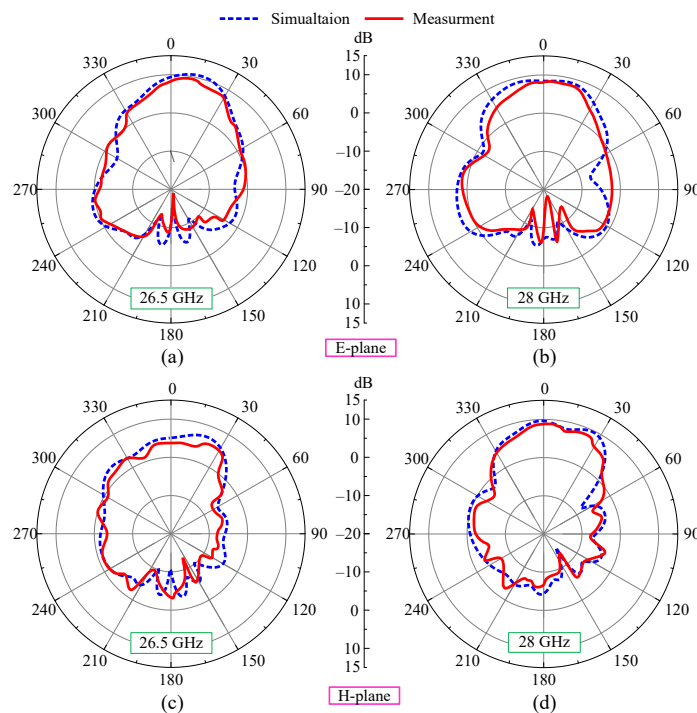


**Figure 17.** Comparison of measured and simulated results of the MIMO system: (a) 26.5 GHz and (b) 28 GHz at E-plane, and (c) 26.5 GHz and (d) 28 GHz at H-plane.

### 3.4. ECC

The Envelope Correlation Coefficient ( $\rho_{eij}$ ) determines whether each individual antenna element phase is independent for the MIMO system. Ideally, the ECC must be zero for a perfect MIMO antenna system; however, due to the losses in materials and nature, an ECC value of less than 0.5 is acceptable. The ECC is determined by the means of S-parameters, so it is a unitless quantity. For any MIMO antenna system, the ECC can be calculated using the following expression, as explained in [23]:

$$\rho_{eij} = \frac{|S_{12}S_{11}^* + S_{22}S_{21}^*|^2}{\left[1 - (|S_{11}|^2 + |S_{21}|^2)\right]\left[1 - (|S_{22}|^2 + |S_{21}|^2)\right]} \tag{6}$$

The simulated and measured values of s-parameters are used to evaluate the ECC; the comparison of both results is shown in Figure 18. Both results offer a very low ECC value, which is close to 0 and less than 0.004.

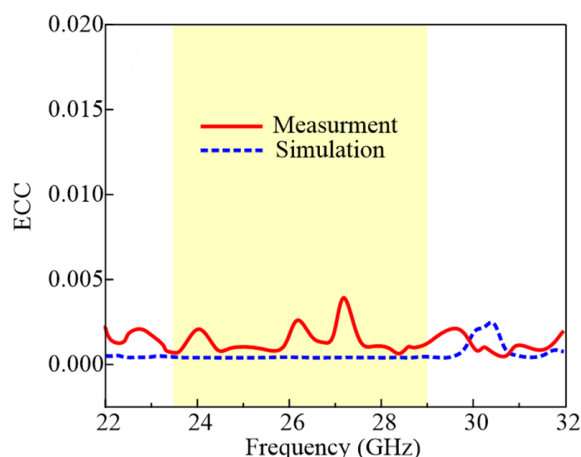


Figure 18. Simulated and measured ECC of the proposed PRS-loaded MIMO antenna.

### 3.5. Diversity Gain

Diversity gain is the loss of transmission power when diversity schemes are performed on modules for MIMO configurations; this is calculated from the above formula, as cited in the reference. The graph shown as ECC shows that DG is 9.99 dB over the entire communication band of the antenna, as shown in Figure 19. This shows that the antenna has excellent diversity performance.

$$DG = 10\sqrt{1 - |\rho_{eij}|^2} \tag{7}$$

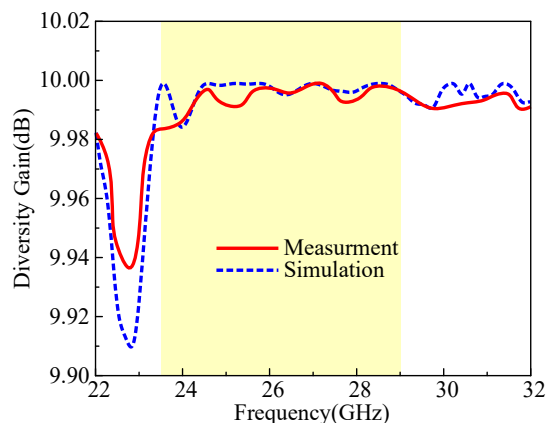


Figure 19. Simulated and measured DG of proposed PRS-loaded MIMO antenna.

### 3.6. CCL (Channel Capacity Loss)

CCL stands for Channel Capacity Loss, which occurs when a wireless communication system's receiver receives a signal. In an MIMO system, the receiver, equipped with multiple antennas, captures signals from various paths simultaneously. The presence of interference between antennas becomes evident through variations in the CCL. An antenna's performance directly influences CCL, with better antenna performance leading to lower CCL values. As the distance between the receiver and antenna decreases, CCL tends to increase. Additionally, the characteristics of the channel can also impact CCL. Consequently, CCL serves as a performance metric for evaluating MIMO antenna efficiency and should ideally be minimal to mitigate errors stemming from other factors. Mathematically, CCL is computed using the following expressions [24]:

$$C(loss) = -\log_2 \det(a) \quad (8)$$

$$a = \begin{bmatrix} \sigma_{11} & \sigma_{12} \\ \sigma_{21} & \sigma_{22} \end{bmatrix} \quad (9)$$

$$\sigma_{ii} = 1 - (|S_{ii}|^2 - |S_{ij}|^2) \quad (10)$$

$$\sigma_{ij} = -(S_{ii}^* S_{ij} + S_{ji} S_{jj}^*) \quad (11)$$

For the operational band, the proposed antenna offers a low CCL of <0.4 bits/s/Hz for both simulated and measured results, as shown in Figure 20.

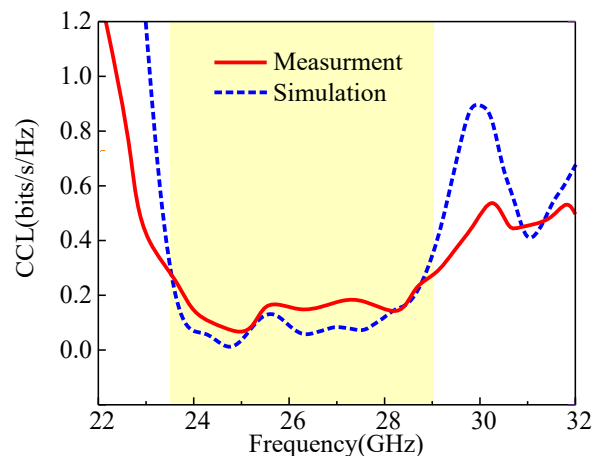


**Figure 20.** Simulated and measured CCL of proposed PRS-loaded MIMO antenna.

### 3.7. Comparison with Related Work

The performance comparison of the proposed work in terms of size, bandwidth, mutual coupling,  $-3$  dB bandwidth and efficiency is performed with the recently reported work. Except from the work reported in [7,11], the proposed work overperformed in comparison with the other work in terms of size. Moreover, the work reported in [7,11] offers a narrow bandwidth, high mutual coupling and low gain as compared to the proposed work. Only the work reported in [8] offers the peak high-gain value of around 18 dBi, at the cost of twice the size of the proposed antenna. Thus, it can be concluded that the proposed PRS-loaded MIMO antenna system offers a good combination of various performance parameters by exhibiting a compact size, wideband and high gain, making it a potential candidate for future 5G devices operating using a 28 GHz band spectrum, as shown in Table 2.

**Table 2.** Comparison of proposed PRS-loaded MIMO antenna with related works.

Ref. No.	No. of Ports	Antenna Size (mm × mm)	$ S_{11} $ BW	Isolation (dB)	Max Gain (dBi)	−3 dB Gain BW	Efficiency (%)
[9]	4 (2 × 2)	31 × 48	26~31 GHz	−21	10	26~31 GHz	-
[11]	4 (2 × 2)	32 × 32	27.6~29.1 GHz	−40	10.6	27.6~29.1 GHz	85
[12]	4 (2 × 2)	30 × 30	27~29 GHz	−29	6.1	27~29 GHz	90
[13]	4 (2 × 2)	25 × 25	25.2~28 GHz	−23.2	8.72	-	-
[15]	4 (2 × 2)	30 × 35	25.5~29.6 GHz	−10	8.1	26~29.6 GHz	82
[16]	4 (2 × 2)	22 × 22	23.3~28.8 GHz	−23	10.44	-	80
[25]	4 (2 × 2)	30 × 43	24.5~26.5 GHz	−45	10.27	24.5~26.5 GHz	-
This Antenna	4 (2 × 2)	24 × 24	23.5~29 GHz	−33	11.4	23.6~28.8 GHz	84

#### 4. Conclusions

This paper introduces the design of a high-gain antenna based on PRS and its MIMO configuration, intended for 28 GHz applications. The basic radiator is derived from a conventional circular patch antenna through the incorporation of a pair of vias and a semi-circular slot. Subsequently, a PRS is developed for a similar operational band and positioned on the top side of the antenna with an air gap to enhance radiation characteristics.

The performance enhancement of the PRS-loaded antenna improves the bandwidth from 24.29–28.45 GHz to 23.6~28.8 GHz, accompanied by an elevation in peak gain from 8.3 to 11.4 dBi. To fulfill the requisites of contemporary and future devices utilizing MIMO systems, an MIMO antenna is constructed utilizing four-unit elements, strategically positioned orthogonally. The PRS is also extended to cover the MIMO antenna, maintaining the same distance as that of a unit element. The optimized PRS-loaded MIMO antenna offers a broad frequency range of 23.5–29 GHz and a peak gain of 11.4 dBi. A comprehensive exploration of various MIMO parameters reveals that the proposed work provides low-mutual-coupling and ECC values of less than −33 dB and 0.005, respectively.

Furthermore, a comparative analysis with related works highlights that the proposed PRS-loaded antenna outperforms other alternatives, positioning itself as a robust contender for future mmWave devices requiring high-gain MIMO antenna systems.

**Author Contributions:** Conceptualization, methodology, software, J.J. and W.A.A.; validation, formal analysis, investigation, resources, data curation, D.C., J.L., N.H. and N.K.; writing—original draft preparation, J.J., D.C. and J.L.; writing—review and editing, W.A.A., N.H. and N.K.; supervision, funding acquisition, N.K. All authors have read and agreed to the published version of the manuscript.

**Funding:** This work was supported by the Institute of Information & Communications Technology Planning & Evaluation (IITP) grant funded by the Korea government (MSIT) (No. 2022-0-01031, development of the measured EMF big data analysis and management platform).

**Data Availability Statement:** All data is included in the manuscript.

**Conflicts of Interest:** The authors declare no conflict of interest.

#### References

- Ikram, M.; Sultan, K.; Lateef, M.F.; Alqadami, A.S.M. A Road towards 6G Communication—A Review of 5G Antennas, Arrays, and Wearable Devices. *Electronics* **2022**, *11*, 169. [CrossRef]
- Dangi, R.; Lalwani, P.; Choudhary, G.; You, I.; Pau, G. Study and Investigation on 5G Technology: A Systematic Review. *Sensors* **2022**, *22*, 26. [CrossRef] [PubMed]
- Hussain, N.; Jeong, M.J.; Abbas, A.; Kim, N. Metasurface-based single-layer wideband circularly polarized MIMO antenna for 5G millimeter-wave systems. *IEEE Access* **2020**, *8*, 130293–130304. [CrossRef]
- Boccardi, F.; Heath, R.W.; Lozano, A.; Marzetta, T.L.; Popovski, P. Five disruptive technology directions for 5G. *IEEE Commun. Mag.* **2014**, *52*, 74–80. [CrossRef]
- Lu, L.; Li, G.Y.; Swindlehurst, A.L.; Ashikhmin, A.; Zhang, R. An Overview of Massive MIMO: Benefits and Challenges. *IEEE J. Sel. Top. Signal Process.* **2014**, *8*, 742–758. [CrossRef]
- Cuneray, K.; Akcam, N.; Okan, T.; Arican, G.O. 28/38 GHz dual-band MIMO antenna with wideband and high gain properties for 5G applications. *AEU-Int. J. Electron. Commun.* **2023**, *162*, 154553. [CrossRef]

7. Yang, B.; Yu, Z.; Dong, Y.; Zhou, J.; Hong, W. Compact tapered slot antenna array for 5G millimeter-wave massive MIMO systems. *IEEE Trans. Antennas Propag.* **2017**, *65*, 6721–6727. [[CrossRef](#)]
8. Park, J.S.; Ko, J.-B.; Kwon, H.-K.; Kang, B.-S.; Park, B.; Kim, D. A tilted combined beam antenna for 5G communications using a 28-GHz band. *IEEE Antennas Wirel. Propag. Lett.* **2016**, *15*, 1685–1688. [[CrossRef](#)]
9. Wani, Z.; Abegaonkar, M.P.; Koul, S.K. A 28-GHz antenna for 5G MIMO applications. *Prog. Electromagn. Res. Lett.* **2018**, *78*, 73–79. [[CrossRef](#)]
10. Shoaib, N.; Shoaib, S.; Khattak, R.Y.; Shoaib, I.; Chen, X.; Perwaiz, A. MIMO antennas for smart 5G devices. *IEEE Access* **2018**, *6*, 77014–77021. [[CrossRef](#)]
11. Sufian, M.A.; Hussain, N.; Abbas, A.; Awan, W.A.; Choi, D.; Kim, N. A Series fed Planar Array-based 4-port MIMO Antenna for 5G mmWave IoT Applications. In Proceedings of the Asia-Pacific Microwave Conference (APMC), Yokohama, Japan, 29 November–2 December 2022; pp. 880–882.
12. Kamal, M.M.; Yang, S.; Ren, X.-C.; Altaf, A.; Kiani, S.H.; Anjum, M.R.; Iqbal, A.; Asif, M.; Saeed, S.I. Infinity shell shaped MIMO antenna array for mm-Wave 5G applications. *Electronics* **2021**, *10*, 165. [[CrossRef](#)]
13. Güler, C.; Bayer Keskin, S.E. A Novel High Isolation 4-Port Compact MIMO Antenna with DGS for 5G Applications. *Micromachines* **2023**, *14*, 1309. [[CrossRef](#)] [[PubMed](#)]
14. Pourgholamhossein, Z.; Jazi, M.N.; Denidni, T.A. Broadband flat-lens antenna design using ultrathin Huygens’ metasurface for millimeter-wave applications. *IEEE Trans. Antennas Propag.* **2022**, *4*, 713–723. [[CrossRef](#)]
15. Khalid, M.; Iffat Naqvi, S.; Hussain, N.; Rahman, M.; Fawad; Mirjavadi, S.S.; Khan, M.J.; Amin, Y. 4-port MIMO antenna with defected ground structure for 5G millimeter wave applications. *Electronics* **2020**, *9*, 71. [[CrossRef](#)]
16. Sehrai, D.A.; Asif, M.; Shah, W.A.; Khan, J.; Ullah, I. Metasurface-based wideband MIMO Antenna for 5G millimeter-wave systems. *IEEE Access* **2021**, *9*, 125348–125357. [[CrossRef](#)]
17. Ferreira-Gomes, B.; Oliveira, O.N., Jr.; Mejía-Salazar, J.R. Chiral Dielectric Metasurfaces for Highly Integrated, Broadband Circularly Polarized Antenna. *Sensors* **2021**, *21*, 2071. [[CrossRef](#)]
18. Balanis, C.A. *Antenna Theory Analysis and Design*, 4th ed.; Wiley: New York, NY, USA, 2016.
19. Dong, G.; Huang, J.; Lin, S.; Chen, Z.; Liu, G. A compact dual-band MIMO antenna for sub-6 GHz 5G terminals. *J. Electromagn. Eng. Sci.* **2022**, *22*, 599–607. [[CrossRef](#)]
20. Mankong, U.; Chamsuk, P.; Nakprasert, S.; Potha, S.; Weng, Z.-K.; Dat, P.T.; Kanno, A.; Kawanishi, T. Millimeter Wave Attenuation Due to Wind and Heavy Rain in a Tropical Region. *Sensors* **2023**, *23*, 2532. [[CrossRef](#)]
21. Park, S.-H.; Jang, G.-H.; Seo, Y.-H.; Keum, H.-S.; Bang, S.-I. High-Speed Antenna Measurement System Using Multi-Probe Array Technique for 5G Applications. *Electronics* **2022**, *11*, 3435. [[CrossRef](#)]
22. Liu, L.; Weng, Y.F.; Cheung, S.W.; Yuk, T.I.; Foged, L.J. Modeling of cable for measurements of small monopole antennas. In Proceedings of the Loughborough Antennas & Propagation Conference, Loughborough, UK, 14–15 November 2011.
23. Lee, J.N.; Hyun, S.B.; Cho, Y.K. A Compact Ultra-Wideband Chip Antenna with Bandwidth Extension Patch and Simple Isolator for MIMO Systems for Mobile Handheld Terminals. *J. Electromagn. Eng. Sci.* **2022**, *22*, 272–282. [[CrossRef](#)]
24. Chae, S.H.; Oh, S.-K.; Park, S.-O. Analysis of Mutual Coupling, Correlations, and TARC in WiBro MIMO Array Antenna. *IEEE Antennas Wirel. Propag. Lett.* **2007**, *6*, 122–125. [[CrossRef](#)]
25. Tariq, S.; Naqvi, S.I.; Will, N.; Amin, Y. A Metasurface-Based MIMO Antenna for 5G Millimeter-Wave Applications. *IEEE Access* **2021**, *9*, 51805–51817. [[CrossRef](#)]

**Disclaimer/Publisher’s Note:** The statements, opinions and data contained in all publications are solely those of the individual author(s) and contributor(s) and not of MDPI and/or the editor(s). MDPI and/or the editor(s) disclaim responsibility for any injury to people or property resulting from any ideas, methods, instructions or products referred to in the content.